AIP Advances ARTICLE pubs.aip.org/aip/adv

Exploration and examination of the structural, optical, thermal, and functional attributes of a hydroxyapatite and cobalt ferrite nanocomposite for biomedical utilization

Cite as: AIP Advances 14, 075026 (2024); doi: 10.1063/5.0214715
Submitted: 19 April 2024 • Accepted: 9 July 2024 •
Published Online: 25 July 2024

Md. Arif Hossain,[1,2,a] Nilufer Yesmin Tanisa,[2] Rabiul Awal,[2] Md. Ifat-Al-Karim,[3] Md. Mominul Islam,[1] Md. Mahbubul Haque,[4] and Md. Mahmudur Rahman[2]

AFFILIATIONS

[1] Department of Physics, Hajee Mohammad Danesh Science and Technology University, Dinajpur 5200, Bangladesh
[2] Department of Physics, Uttara University, Uttara 1230, Bangladesh
[3] Physics Discipline, Khulna University, Khulna 9208, Bangladesh
[4] Materials Science Division, Atomic Energy Centre, Dhaka 1000, Bangladesh

[a] **Author to whom correspondence should be addressed:** arifphy636@gmail.com

ABSTRACT

Hydroxyapatite (Hap) is a cornerstone material in biomedical fields, crucial for bone tissue repair and replacement in the human body. However, its mechanical strength falls short compared to that of natural bone, necessitating enhancements. Addressing this challenge, cobalt ferrite emerges as a promising reinforcing agent for Hap, boasting excellent biocompatibility. Diffraction was employed to assess the crystallinity and phase purity of hydroxyapatite, cobalt ferrite, and the composite. The results indicated a crystallite size of 13.51 nm for hydroxyapatite, 9.62 nm for cobalt ferrite, and 76.4 nm for the hydroxyapatite/cobalt ferrite composite. Further characterization through Fourier Transform Infrared Spectroscopy (FTIR) and Raman spectroscopy confirmed the presence of functional groups in the synthesized materials. FTIR analysis validated the successful synthesis of hydroxyapatite, cobalt ferrite, and their composite. Specifically, FTIR spectra exhibited oxygen functional groups such as –OH, –CO, C=O, and C–OH in hydroxyapatite, while cobalt ferrite exhibited CO_2, Fe–O, and Co–O groups. Ultraviolet analysis was conducted to determine the bandgap energies, revealing values of 3.51 eV for cobalt ferrite and 5.47 eV for hydroxyapatite. This comprehensive characterization underscores the potential of the Hap/$CoFe_2O_4$ nanocomposite in bone tissue engineering.

I. INTRODUCTION

Hap stands out as a highly versatile biomaterial employed in implantation and grafting, owing to its remarkable resemblance to the composition of teeth and bone tissues. Its chemical makeup is represented by the formula $Ca_{10}(PO_4)_6(OH)_2$.[1] Essential characteristics defining a biomaterial encompass bioactivity, non-inflammatory properties, biocompatibility, osteoconductivity, safety, and non-immunogenicity.[2] Fortunately, the array of attributes found in Hap mirror those of calcium phosphates present in human bone, establishing its biocompatibility with these tissues. Consequently, Hap stands as a pivotal material in biomedicine.[3] Its versatility finds expression in the reconstruction of skull defects,[4] the rectification of substantial bone defects, and the burgeoning field of bone tissue engineering.[5] Moreover, HAP plays a crucial role in the removal of heavy metals from biological systems,[6] and notably, it serves as a potent vehicle for drug delivery.[7] As nanotechnology continues to advance, scientists have undertaken significant endeavors to diversify the morphologies of Hap, broadening the scope of the Hap family and enhancing its applicability.[8] This relentless pursuit of innovation not only enriches our understanding of Hap but also opens avenues for novel applications across var-

ious disciplines, promising transformative solutions in medicine, environmental remediation, and beyond.

Magnetic nano-materials have emerged as invaluable assets across a spectrum of applications, ranging from catalysis[9] and colloidal photonic crystals[10] to magnetic particle imaging,[11] nanofluids,[12] data storage,[13] defect sensors,[14] optical filters,[15] and environmental remediation.[16] Their versatility knows no bounds. Especially noteworthy is their potential in the biomedical industry, where magnetic nanoparticles stand out due to their unparalleled mechanical, thermal, physical, and chemical attributes.[17] Over recent decades, there has been a surge in the development of nanocomposite particles combining hydroxyapatite (Hap) with magnetic materials such as Fe_3O_4, γFe_2O_3, $CoFe_2O_4$, $MnFe_2O_4$, or $MgFe_2O_4$, specifically tailored for biomedical applications such as drug delivery systems, catalysts, and hyperthermia agents. These materials boast biocompatibility and exhibit unique magnetic properties.[18–22] Among the plethora of ferrite materials explored for magnetic recording applications, cobalt ferrite ($CoFe_2O_4$) stands out for its exceptional chemical stability and mechanical hardness, making it a prime candidate for such purposes.[23] Its widespread consideration underscores its significance in advancing magnetic recording technologies. Finally, the convergence of hydroxyapatite (Hap) with magnetic materials has unveiled a new era in biomedical engineering, offering a myriad of opportunities for drug delivery, catalysis, and hyperthermia treatments. With a foundation rooted in the exceptional biocompatibility and unique magnetic properties of these composite materials, their potential spans across diverse fields, from medicine to environmental remediation. As cobalt ferrite ($CoFe_2O_4$) emerges as a standout contender among ferrite materials for magnetic recording applications, it epitomizes the fusion of cutting-edge technology with inherent material properties, promising transformative solutions in the realm of magnetic recording technologies. As research in this field continues to evolve, the synergistic potential of HAP-magnetic nanocomposites remains poised to revolutionize various sectors, shaping the landscape of innovation for years to come.

II. METHODOLOGY

A. Synthesis of hydroxyapatite

The synthesis of hydroxyapatite $Ca_{10}(PO4)_6(OH)_2$ nanoparticles involved utilizing 0.5M solutions of $Ca(NO_3)_2.4H_2O$ and $(NH_4)_2HPO_4$ as precursor materials. A co-precipitation agent, 3.0M NaOH, was employed. The precursor solutions were prepared by dissolving the respective salts in deionized water. Subsequently, the solutions were combined under continuous stirring. After stirring for about 2 h, NaOH (3M) was slowly added dropwise to maintain the pH at 10.00.[24] The mixture was then subjected to centrifugation at 12 000 rpm for 20 min. The resulting precipitate was dried to obtain the desired hydroxyapatite nanoparticles. The chemical reactions involved in the production of $Ca_{10}(PO_4)_6(OH)_2$ nanoparticles are provided below:

$$10\,Ca(NO_3)_2 \cdot 4H_2O + 6(NH_4)_2\,HPO_4 + 2H_2O = Ca_{10}(PO_4)_6(OH)_2 + 12\,NH_4\,NO_3 + 8\,HNO_3.$$

B. Synthesis of cobalt ferrite

To synthesize cobalt ferrite, $CoC_{l2}.6H_2O$, $FeCl_3$, and NaOH are dissolved in deionized water. The salt solutions are combined in a beaker and stirred using a magnetic stirrer. NaOH solution is gradually added dropwise to the salt solution to regulate the pH, which is maintained between 11 and 12 throughout the reaction. The reactants are continuously stirred until the desired pH is achieved. The resulting product is washed with deionized water and centrifuged multiple times at 13 000 rpm for 20 min, leaving behind a thick black precipitate. This precipitate is then dried at 80 °C for 72 h.[25] The dried substance is subsequently ground into a fine powder. MNP properties such as morphology, particle size, chemical composition, and magnetic properties depend on the synthesis method and conditions, for example, temperature, PH, etc. The stoichiometric reaction for the synthesis of cobalt ferrite ($CoFe_2O_4$) is as follows:

$$CoCl_2 \cdot 6H_2O + 2FeC_{l3} + NaOH = CoFe_2O_4 + 8\,NaCl + 10H_2O.$$

C. Method for producing hydroxyapatite and cobalt ferrite

Experiments exploring lower weight ratios of $CoFe_2O_4$ ranging from 4 to 8 wt. % were conducted. Here, different percentage ratios were chosen to show comparison for different concentrations. Hydroxyapatite (Hap) powders were blended with $CoFe_2O_4$ at various Hap/$CoFe_2O_4$ weight ratios (4%, 6%, and 8%). The mixture was then placed into stainless steel vials along with stainless steel balls (10 mm in diameter) at a powder/ball mass ratio of 1:10. The milling process lasted for 10 min, followed by sintering at 1200 °C for 3 h.[26]

III. CHARACTERIZATION

A. X-ray diffraction analysis

Figure 1(a) illustrates the x-ray diffraction spectra for hydroxyapatite, revealing distinct peaks corresponding to the crystal planes (002), (211), (300), (202), (310), (222), (213), (004), and (304). These peaks serve as unequivocal evidence for the formation of a polycrystalline structure within the HAP nanoparticles, as documented in Ref. 27. In Fig. 1(b), the x-ray diffraction patterns for cobalt ferrite are depicted, showcasing characteristic peaks attributed to the crystal planes (220), (311), (400), and (511). These peaks decisively affirm the presence of a polycrystalline structure within cobalt ferrite, as cited in Ref. 28. The x-ray diffraction spectra presented in Figs. 1(c)–1(e) correspond to the HAP/cobalt ferrite composite. Notably, the sole observation of the (311) plane in the $CoFe_2O_4$ phase within the Hap/$CoFe_2O_4$ composite underscores its distinct crystalline nature. Moreover, a meticulous comparison of the obtained XRD patterns with the standard Hap and $CoFe_2O_4$ phases reveals a remarkable congruence in peak positions, as detailed in Ref. 29. This coherence further validates the successful formation of the composite material.

In our research endeavors, we delved into exploring the crystallite dimensions of various materials. Specifically, we found that the crystallite size of hydroxyapatite (Hap) stood at 13.71 nm, while that of cobalt ferrite ($CoFe_2O_4$) measured 9.62 nm. Interestingly, the hybrid material comprising both Hap and $CoFe_2O_4$ exhibited

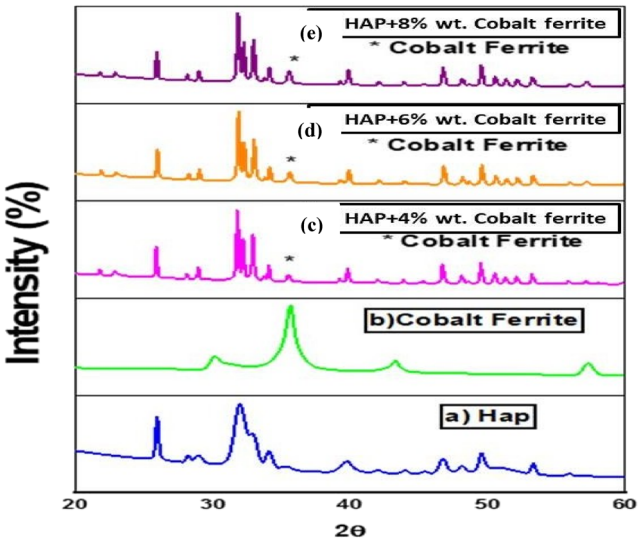

FIG. 1. XRD pattern of (a) hydroxyapatite, (b) cobalt ferrite, (c) Hap + 4 wt. % cobalt ferrite, (d) Hap + 6 wt. % cobalt ferrite, and (e) Hap + 8 wt. % cobalt ferrite.

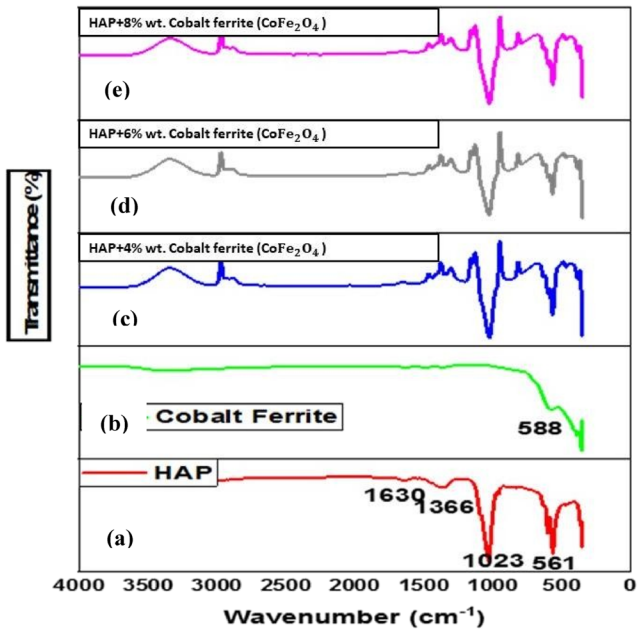

FIG. 2. FTIR pattern of (a) hydroxyapatite, (b) cobalt ferrite, (c) HAP + 4 wt. % cobalt ferrite, (d) HAP + 6 wt. % cobalt ferrite, and (e) HAP + 8 wt. % cobalt ferrite.

a significantly larger crystallite size, amounting to 76.4 nm. These determinations were made utilizing the Debye–Scherrer formula, a fundamental tool in crystallography.[30]

The Debye–Scherrer formula is expressed as

$$D = K\lambda/\beta \cos\theta.$$

Here, λ represents the wavelength of x rays (Cu Kα = 0.154 nm), while D signifies the crystal its size in nanometers. In addition, β denotes the full width at half maximum (FWHM), measured in radians, and θ represents the angle of diffraction, also measured in radians. The constant K, a crystallite shape factor, played a crucial role in our computations, with a value of k = 0.9.

B. Fourier transform infrared spectroscopy (FTIR) analysis

The prominent functional groups identified in the Fourier Transform Infrared (FTIR) spectrum of synthesized hydroxyapatite (HAP) include the phosphate group (PO_4^{3-}), hydroxyl group (OH), and carbonate group (CO_3^{2-}).[31] Within this spectrum, the stretching modes of hydroxyl groups appear at around 3372–3348 cm^{-1}, while the absorption attributed to adsorbed water manifests as a broad peak. Notably, the O–H stretch vibration of hydrogen-bonded –OH groups is evident in the range of 3300–2300 cm^{-1}, particularly observed at 2990 cm^{-1}. In addition, a significant indicator of the presence of OH groups within the HAP lattice is the stretching mode of O–H, typically observed at around 3600–3300 cm^{-1},[32] with a specific instance noted at 3369 cm^{-1}. In contrast, the FTIR spectrum of the cobalt ferrite sample [Fig. 2(b)] displays a distinct broadband at 588 cm^{-1}, attributed to the intrinsic Co–O stretching vibration, indicating the presence of spinel ferrites. Furthermore, peaks within the range of 950–1155 cm^{-1} are associated with the Fe–Co alloy system,[33,34] with the specific bond at 1068 cm^{-1} attributed to Fe–Co. Moreover, the presence of the NO_3 group is characterized by a symmetric vibration observed at 1364 cm^{-1}, while O–H stretching vibrations are discernible at 3420 and 2977 cm^{-1}, and an absorption band at 1630 cm^{-1} corresponds to the bending of absorbed water molecules.[35] Figures 2(c)–2(e) depict the chemical structure and functional groups of Hap/$CoFe_2O_4$ composites with varying $CoFe_2O_4$ weight ratios, examined through FT-IR spectroscopy. The analysis reveals overlapping of the $CoFe_2O_4$ and Hap bands, resulting in the disappearance of the $CoFe_2O_4$ band at 588 cm^{-1} in the composite spectrum. Despite this, a consistent pattern in the FT-IR spectra is observed across all composite conditions. Notably, the addition of $CoFe_2O_4$ introduces variations in intensity and shift of Hap bands, indicative of interactions between Hap and $CoFe_2O_4$ phases.

C. Ultra-violet analysis for estimation of optical bandgap energy

The calculated optical bandgap of $CoFe_2O_4$ is 3.51 eV, as shown in Fig. 3(b), and the bandgap energy for the prepared hydroxyapatite sample is 5.47 eV, as shown in Fig. 3(a). In addition, the Tauc and Wood plot is given by

$$\alpha h\nu = B(h\nu - Eg)^n,$$

where α is the absorbance of the sample, hvis the incident energy of the photon, E_g is the optical bandgap, n is an exponent, and B is a band tailoring constant.[36]

It can be shown that the bandgap energy of HAP is large compared to that of cobalt ferrite. The composite does not show a relevant graph for the determination of bandgap energy. These results indicate a shift in the optical bandgap, possibly due to structural phase transformations. This observation aligns with findings

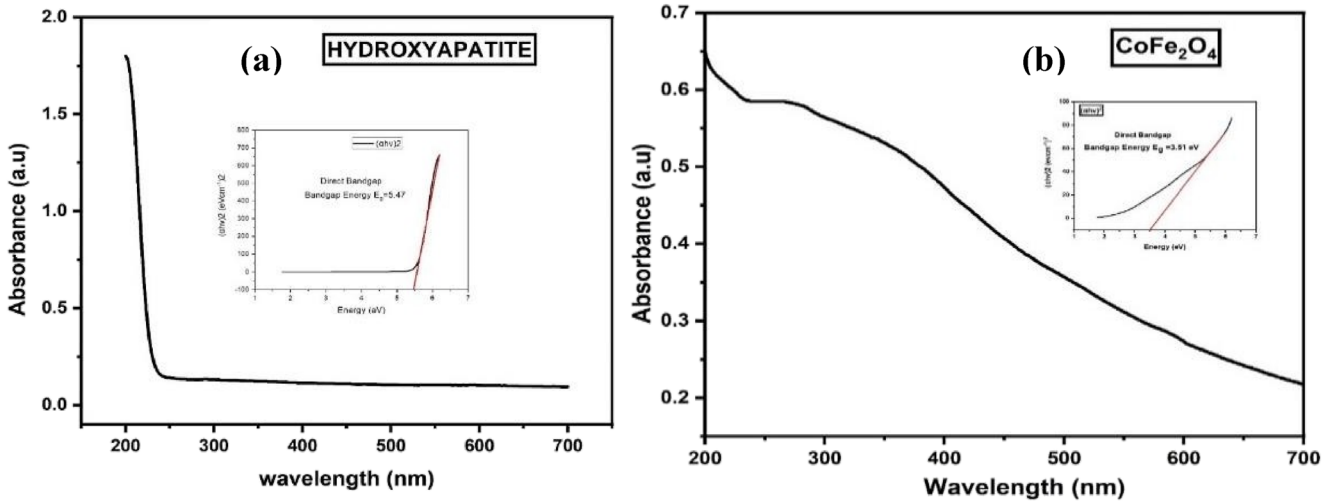

FIG. 3. UV analysis of (a) hydroxyapatite and (b) cobalt ferrite.

reported by various researchers.[34,35] A crucial observation is that the bandgap tends to increase with a reduction in particle size. This phenomenon can be attributed to the absorption of light, which results from the excitation of electrons from the valence band to the conduction band. This behavior is central to the determination of the bandgap through the aforementioned method.[37,38]

D. Raman spectroscopy analysis

Figure 4 illustrates the Raman spectra obtained from both hydroxyapatite (Hap) and Hap/cobalt ferrite samples. In the spectrum of Hap, a distinctive Raman peak is detected within the range of 963–961 cm^{-1}, which has been previously attributed to the v1 PO_4^{3-} mode.[39,40] Notably, a similar peak is discernible at ~965 cm^{-1} in the Hap samples under investigation. Furthermore, the presence of three additional PO_4^{3-} modes is evident in the spectra, spanning the regions of 450–400 cm^{-1} (PO_4^{3-} v2), 1076–1028 cm^{-1} (PO_4^{3-} v3), and 610–579 cm^{-1} (PO_4^{3-} v4),[41,42] as depicted in Fig. 4. Consequently, the Raman peak observed at around 1051 cm^{-1} in the HAP samples can be attributed to the PO_4^{3-} (v3) mode.[38,39] The bandwidth around 965 cm^{-1} in the spectrum of Hap appears notably broader than the other bandwidths observed in the Hap samples. This discrepancy suggests a higher likelihood of a comparatively elevated CO_3^{2-} content within the Hap sample.[43] However, in the case of the Hap/cobalt ferrite composite, no discernible peak corresponding to cobalt ferrite is detected, akin to the finding in the FTIR analysis.

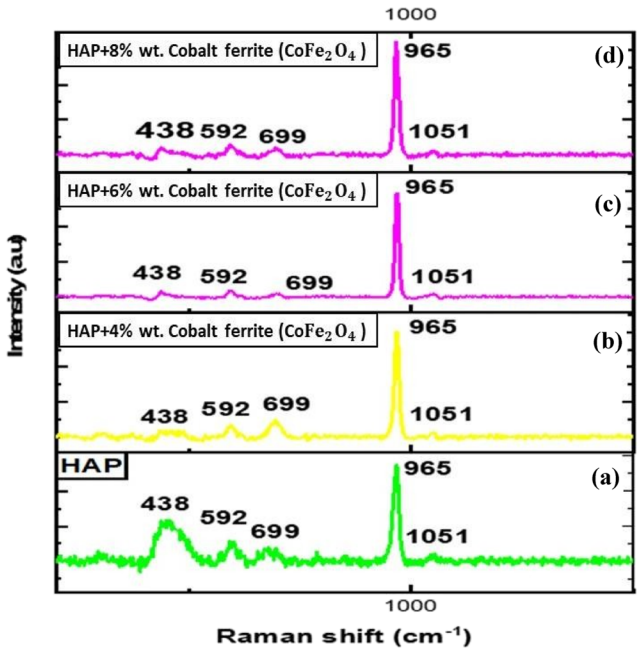

FIG. 4. Raman analysis of (a) hydroxyapatite, (b) 4 wt. % cobalt ferrite + Hap, (c) 6 wt. % cobalt ferrite + Hap, and (d) 8 wt. % cobalt ferrite + Hap.

E. TEM analysis

Figure 5 presents TEM images, particle size distribution histograms, and selected area electron diffraction (SAED) patterns of synthesized HAP/$CoFe_2O_4$ composites. From the TEM images shown in Fig. 5(a), there are lots of defect sites that can be observed on the surface of the composite as well as explained nanoparticles. The particle size distribution histogram was constructed based on the analysis of 40 nanoparticles. As shown in Fig. 5(b), the mean size of the HAP/$CoFe_2O_4$ composite particles is 64 nm with a standard deviation of 11 nm. Furthermore, a noticeable reduction in agglomeration is observed, and smaller-sized particles are fabricated. From XRD analysis, by applying the Debye–Scherrer equation, the average crystalline size of the HAP/$CoFe_2O_4$ nanoparticles is reported as

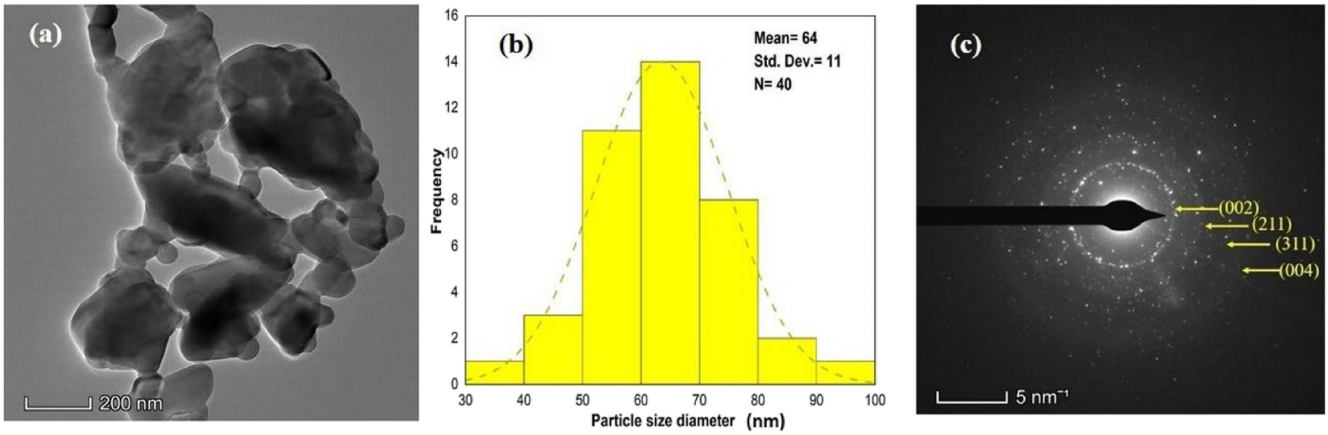

FIG. 5. (a) TEM images of HAP/$CoFe_2O_4$ composites, (b) particle size distribution histogram of HAP/$CoFe_2O_4$ composites, and (c) SAED pattern of HAP/$CoFe_2O_4$ composites.

76.4 nm, which is in an agreement with the result obtained from the TEM images.[44,45]

The selected area electron diffraction (SAED) pattern supports this, indicating a fully crystalline structure with multiple lattice plane reflections. In the SAED pattern of the HAP/$CoFe_2O_4$ composites shown in Fig. 5(c), concentric circles are observed for HAP, indexed as (002), (211), and (004) lattice planes, and concentric circles are observed for cobalt ferrite, indexed as (311). These circles

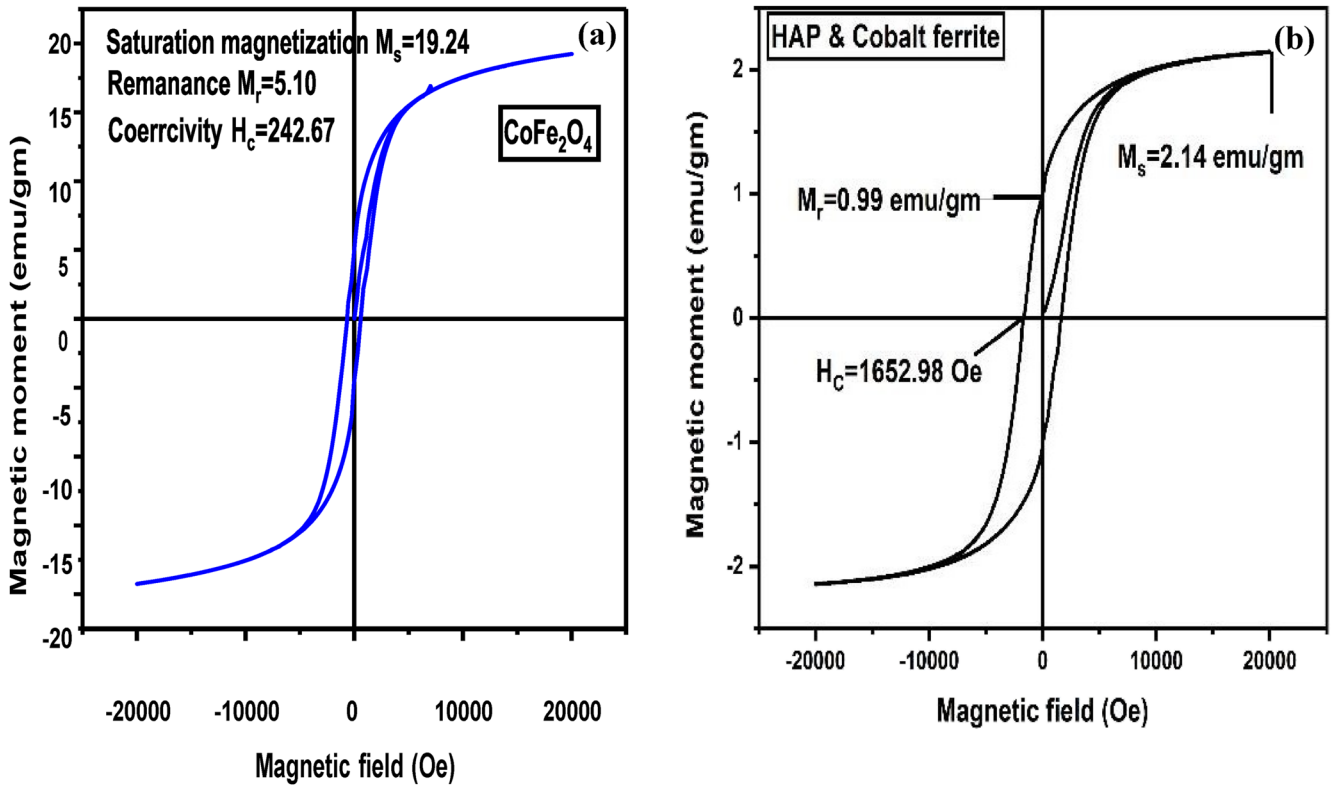

FIG. 6. VSM analysis of (a) cobalt ferrite and (b) Hap/cobalt ferrite composite.

Table I. Magnetization (MS), remanence (Mr), and coercivity (Hc) for Hap and the Hap/cobalt ferrite composite.

Sample	Magnetization (M_S)	Remanence (M_r)	Coercivity (H_c)	Remanence ratio ($R = M_r/M_s$)
Cobalt ferrite	19.24	5.10	242.67	0.27
Hap/cobalt ferrite	2.14	0.99	1652.98	0.46

correspond well with the XRD data. Therefore, the SAED pattern indicates that synthesized HAP/$CoFe_2O_4$ nanoparticles possess a fully crystalline structure. A comparative assessment between TEM images and XRD studies indicates that the synthesized composites significantly influence nanoparticle size, playing a crucial role in controlling the size reduction process.

F. Vibrating sample magnetometer analysis

According to the data presented in Fig. 6, the saturation magnetization for cobalt ferrite is calculated to be 19.24 emu/g, as shown in Fig. 6(a), significantly lower than the reported value for bulk cobalt ferrite (74.08 emu/g).[46] Conversely, hydroxyapatite (Hap) exhibits no discernible magnetic properties on its own. However, when combined with cobalt ferrite, Hap demonstrates magnetic behavior, with the saturation magnetization recorded at 2.14 emu/gm for the composite material, as shown in Fig. 6(b). The degree of intergrain group exchanges, determined by the parameter R ranging from 0 to 1, signifies the presence or absence of various types of interactions.[47] For instance, $R < 0.5$ indicates particle interaction primarily through magneto-static forces, while $R = 0.5$ suggests randomly oriented non-interacting particles undergoing coherent rotations.[48,49] Values of $1 > R > 0.5$ confirm the existence of exchange-coupling particles. The observed R values below 0.5 for both cobalt ferrite and Hap/cobalt ferrite samples suggest predominant interactions via magneto-static mechanisms. The fluctuations in the coercivity field

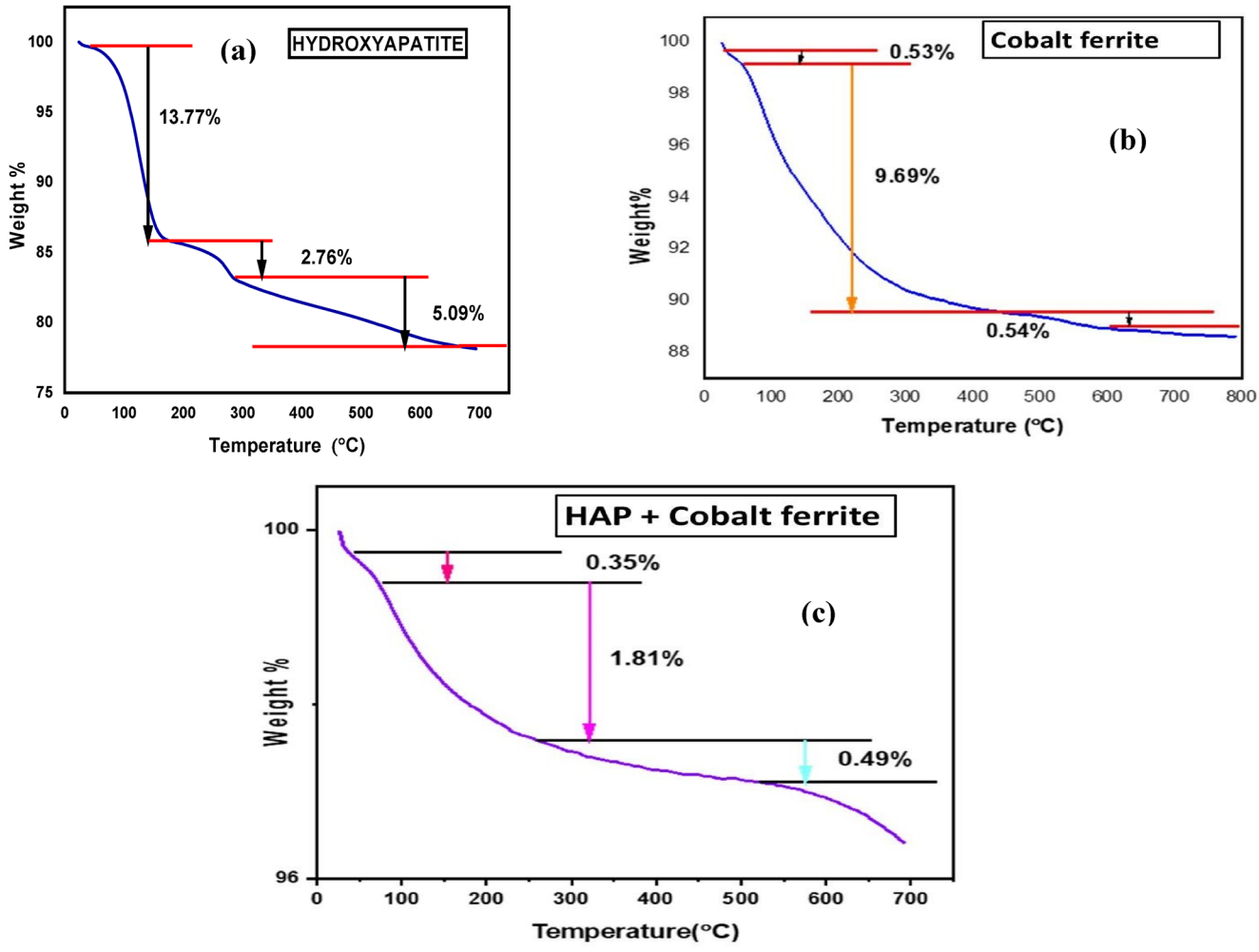

FIG. 7. TGA analysis of (a) hydroxyapatite, (b) cobalt ferrite, and (c) Hap/cobalt ferrite.

and remanence ratio with particle size can be elucidated by considering factors such as domain structure, critical size, and crystal anisotropy.[50] These parameters influence the magnetic properties and behavior of the materials under investigation. Table I shows the magnetization (MS), remanence (Mr), and coercivity (Hc) for the Hap and Hap/cobalt ferrite composite.

G. Thermogravimetric analysis (TGA) analysis

The TGA curves depicted in Figs. 7(a)–7(c) illustrate the thermal behavior of the respective samples. Beginning with the as-prepared Hap sample, as indicated in Fig. 7(a), the TGA analysis revealed a gradual weight loss pattern. Specifically, there was a recorded weight loss of 13.77% between 40 and 170 °C, followed by additional weight losses of 2.76% between 170 and 290 °C and 5.09% from 170 to 680 °C. This weight loss profile suggests successive stages of decomposition or chemical transformations occurring within the sample across varying temperature ranges. Moreover, for the $CoFe_2O_4$ sample showcased in Fig. 7(b), a distinct thermal degradation pattern was observed. The TGA curve exhibited a minor initial weight loss of 0.53% between 32 and 445 °C, followed by a slight increase in weight loss of 0.54% from 445 to 601 °C. These observations suggest specific thermal events or phase transitions unique to the $CoFe_2O_4$ sample, possibly associated with its chemical composition or structural properties. Moving on to the TGA curve of the as-prepared Hap sample presented in Fig. 7(c), a nuanced weight loss profile emerged. Within the temperature range of 37–73 °C, a minor weight loss of 0.35% was observed, followed by a more substantial weight loss of 1.81% from 73 to 257 °C. In addition, a further weight loss of 0.49% occurred between 170 and 680 °C. Notably, the weight loss observed below 180 °C was attributed to the dehydration of absorbed moisture, while the subsequent weight loss up to 500 °C was attributed to the removal of crystal water and surfactant from the sample.[51–53]

IV. CONCLUSION

To further advance the biomedical utilization of hydroxyapatite, it is imperative to enhance its structural and mechanical characteristics. In pursuit of this enhancement, cobalt ferrite was chosen due to its exceptional compatibility and bioactivity, leading to the successful synthesis of the hydroxyapatite/cobalt ferrite composite, in the characterization of the synthesized samples.

The magnetic properties and hysteresis loop were analyzed using a Vibrating Sample Magnetometer (VSM). Notably, the VSM study revealed that pure hydroxyapatite lacks a hysteresis loop, whereas the incorporation of cobalt ferrite imparts magnetic properties to the composite, aligning with the primary objective of our research. In addition, Thermogravimetric Analysis (TGA) elucidated the weight mass loss behavior with temperature, providing further insights into the thermal stability of the synthesized materials. This result leads to other research opportunities, for example, hydroxyapatite forming compositions with magnesium ferrite, nickel ferrite, etc.

ACKNOWLEDGMENTS

The authors would like to thank the Department of Physics, Hajee Mohammad Danesh Science and Technology University, Dinajpur, for providing the opportunity. Our deepest appreciation extends to the Materials Science Division, Atomic Energy Center, Dhaka, for providing laboratory work and characterization facilities. This research work has been carried out to partially fulfill the degree of Master of Science. This research was not supported or funded by any organization or individuals. The authors are responsible for covering the expenses.

AUTHOR DECLARATIONS

Conflict of Interest

The authors have no conflicts to disclose.

Author Contributions

Md. Arif Hossain: Data curation (equal); Methodology (equal); Resources (equal); Software (equal); Writing – original draft (equal); Writing – review & editing (equal). **Nilufer Yesmin Tanisa**: Investigation (equal); Visualization (equal); Writing – review & editing (equal). **Rabiul Awal**: Investigation (equal); Software (equal); Visualization (equal); Writing – review & editing (equal). **Md. Ifat-Al-Karim**: Software (equal); Writing – review & editing (equal). **Md. Mominul Islam**: Investigation (equal); Supervision (equal); Validation (equal). **Md. Mahbubul Haque**: Investigation (equal); Supervision (equal); Validation (equal). **Md. Mahmudur Rahman**: Funding acquisition (equal); Resources (equal).

DATA AVAILABILITY

I declare that the collected data are original and authors collected all the data.

REFERENCES

[1] A. Galotta, "Low temperature synthesis and cold sintering of natural source derived hydroxyapatite for bone tissue engineering applications," Ph.D. dissertation (University of Trento, 2023).
[2] G. Magnaterra, "Additive manufacturing of hydroxyapatite scaffolds for bone repair," Ph.D. dissertation (Politecnico di Torino, 2020).
[3] K. Alorku, M. Manoj, and A. Yuan, "A plant-mediated synthesis of nanostructured hydroxyapatite for biomedical applications: A review," RSC Adv. **10**, 40923–40939 (2020).
[4] A. Santra and P. Ganguly, "3D bioprinting: Process, techniques, biomaterials and bioinks and its future aspects," Int. J. Chem. Environ. Sci. **4**(4), 46–63 (2023).
[5] A. Veiga, F. Castro, F. Rocha, and A. L. Oliveira, "Protein-based hydroxyapatite materials: Tuning composition toward biomedical applications," ACS Appl. Bio Mater. **3**, 3441–3455 (2020).
[6] G. Wei, C. Gong, K. Hu, Y. Wang, and Y. Zhang, "Biomimetic hydroxyapatite on graphene supports for biomedical applications: A review," Nanomaterials **9**, 1435–1454 (2019).
[7] D. Predoi, S. L. Iconaru, M. V. Predoi, A. Groza, S. Gaiaschi, K. Rokosz, S. Raaen, C. C. Negrila, A.-M. Prodan, A. Costescu, M. L. Badea, and P. Chapon, "Development of cerium-doped hydroxyapatite coatings with antimicrobial properties for biomedical applications," Coatings **10**, 516–532 (2020).
[8] S. R. Bakshi, A. Lahiri, and A. Agarwal, "Carbon nanotube reinforced metal matrix composites: A review," Int. Mater. Rev. **55**, 41–64 (2010).
[9] A. A. Oluwasanu, J. A. Teslim, T. T. Isaiah, I. A. Olalekan, O. A. Chris, and A. C. Ogunyele, "Scientific applications and prospects of nanomaterials: A multidisciplinary review," Afr. J. Biotechnol. **18**(30), 946–961 (2019).

[10] *Advances in Smart Nanomaterials and Their Applications*, edited by A. Husen and K. S. Siddiqi (Elsevier, 2023).
[11] C. Verma, D. K. Verma, E. Berdimurodov, I. Barsoum, A. Alfantazi, and C. M. Hussain, "Green magnetic nanoparticles: A comprehensive review of recent progress in biomedical and environmental applications," J. Mater. Sci. **59**(2), 325–358 (2024).
[12] A. Bouchaala, "Elaboration of new nanomaterials for spintronic applications," Ph.D. dissertation (Université Kasdi Merbah Ouargla, 2024).
[13] M. Abduljawad, "Synthesis and functionalization of hybrid magnetic nanoparticle composites for energy conversion, light harvesting and optical and biomedical applications," Ph.D. Dissertation (The University of Arizona, 2021).
[14] *Industrial Applications of Nanoparticles: A Prospective Overview*, edited by M. I. Litter and A. Ahmad (CRC Press, 2023).
[15] J. Chattopadhyay and N. Srivastava, *Application of Nanomaterials in Chemical Sensors and Biosensors* (CRC Press, 2021).
[16] R. K. Gautam and M. C. Chattopadhyaya, *Nanomaterials for Wastewater Remediation* (Butterworth-Heinemann, 2016).
[17] X. Li, J. Wei, K. E. Aifantis, Y. Fan, Q. Feng, F. Z. Cui, and F. Watari, "Current investigations into magnetic nanoparticles for biomedical applications," J. Biomed. Mater. Res., Part A **104**, 1285–1296 (2016).
[18] N. Petchsang, W. Pon-On, J. H. Hodak, and I. M. Tang, J. Magn. Magn. Mater. **321**, 1990–1995 (2009).
[19] A. Inukai, N. Sakamoto, H. Aono, O. Sakurai, K. Shinozaki, H. Suzuki, and N. Wakiya, J. Magn. Magn. Mater. **323**, 965–969 (2011).
[20] K. H. Zuo, Y. P. Zeng, and D. Jiang, J. Nanosci. Nanotechnol. **12**, 7096–7100 (2012).
[21] H. Jiang, Y. Li, Y. Zuo, W. Yang, L. Zhang, J. Li, L. Wang, Q. Zou, L. Cheng, and J. Li, J. Nanosci. Nanotechnol. **9**, 6844–6850 (2009).
[22] D. Gopi, M. T. Ansaria, E. Shinyjoy, and L. Kavitha, Spectrochim. Acta, Part A **87**, 245–250 (2012).
[23] I. H. Gula, A. Maqsood, M. Naeem, and M. Naeem Ashiq, J. Alloys Compd. **507**, 201–206 (2010).
[24] N. A. S. Mohd Pu', R. H. Abdul Haq, H. Mohd Noh, H. Z. Abdullah, M. I. Idris d, and T. C. Lee, "Synthesis method of hydroxyapatite: A review," Mater. Today: Proc. **29**, 233 (2020).
[25] A. V. Ravindra, M. Chandrika, Ch. Rajesh, P. Kollu, S. Ju, and S. D. Ramarao, "Simple synthesis, structural and optical properties of cobalt ferrite nanoparticles," Eur. Phys. J. Plus **134**, 296 (2019).
[26] P. Klumdounga, A. Hassadeeb, and P. Pankaewc, "Effect of nickel ferrite addition on characteristics of nanostructured nickel ferrite/hydroxyapatite ceramic," Mater. Today: Proc. **17**, 1752–1760 (2019).
[27] R. Klockenkämper, *Chemical Analysis: A Series of Monographs on Analytical Chemistry and Its Applications* (John Wiley and Sons, Inc., 1997), p. 140.
[28] M. H. Fathi and A. Hanifi, Mater. Lett. **61**(18), 3978–3983 (2007).
[29] K. A. Chan and S. G. Kazarian, Chem. Soc. Rev. **45**(7), 1850–1864 (2016).
[30] S. Rana, J. Philip, and B. Raj, Mater. Chem. Phys. **124**, 264 (2010).
[31] P. N. Oliveira, D. M. Silva, G. S. Dias, I. A. Santos, and L. F. Co'tica, Ferroelectrics **499**, 76 (2016).
[32] S. Kangesan, M. Hashim, S. Tamilselvan, N. B. Alitheen, I. Ismail, and G. Bahmanrokh, J. Nanomater. **2013**, 865024.
[33] T. Boobalan, N. Suriyanarayanan, and S. Pavithradevi, Mater. Sci. Semicond. Process. **16**, 1695 (2013).
[34] K. J. Arun, A. K. Batra, A. Krishna, K. Bhat, M. D. Aggarwal *et al.*, "Surfactant free hydrothermal synthesis of copper oxide nanoparticles," Am. J. Mater. Sci. **5**, 36–38 (2015).
[35] B. Radim, "(Photo)electrochemical methods for the determination of the band edge positions of TiO_2-based nanomaterials," Adv. Phys. Chem. **2011**, 786759.
[36] D. Kumar, V. Sudarshan, and A. K. Singh, AIP Conf. Proc. **1953**, 080010 (2018).
[37] V. Polliotto, E. Albanese, S. Livraghi, G. Pacchioni, and E. Giamello, "The photoactive nitrogen impurity in nitrogen-doped zirconium titanate (N–$ZrTiO_4$): A combined electron paramagnetic resonance and density functional theory study," J. Mater. Chem. **5**(25), 13062–13071 (2011).
[38] A. Elisa, V. Cristiana, P. Gianfranco, S. Frédéric, L. Stefano *et al.*, "Nature of paramagnet IC species in nitrogen-doped SnO_2: A combined electron paramagnetic resonance and density functional theory study," J. Phys. Chem. **119**, 26895–26903 (2015).
[39] C. C. Silva, A. G. Pinheiro, M. A. R. Miranda, J. C. Góes, and A. S. B. Sombra, "Structural properties of hydroxyapatite obtained by mechanosynthesis," Solid State Sci. **5**, 553–558 (2003).
[40] F. F. M. De Mul, M. H. J. Hottenhuis, P. Bouter, J. Greve, J. Arends, and J. J. Ten Bosch, "Micro-Raman line broadening in synthetic carbonated hydroxyapatite," J. Dent. Res. **65**, 437–440 (1986).
[41] A. Kalam, A. G. Al-Sehemi, M. Assiri, G. Du, T. Ahmad, I. Ahmad, and M. Pannipara, "Modified solvothermal synthesis of cobalt ferrite ($CoFe_2O_4$) magnetic nanoparticles photocatalysts for degradation of methylene blue with H_2O_2/visible light," Results Phys. **8**, 1046–1053 (2018).
[42] G. Meenal, D. Anushree, M. Satyabratha, D. Dipankar, and D. Anindya, "Surfactant based synthesis and magnetic studies of cobalt ferrite," Appl. Phys. A **126**, 660 (2020).
[43] G. Penel, G. Leroy, C. Rey, and E. Bres, "MicroRaman spectral study of the PO_4 and CO_3 vibrational modes in synthetic and biological apatites," Calcif. Tissue Int. **63**, 475–481 (1998).
[44] R. Awal, M. Al-Mamun, N. Jewena, J. I. Khandaker, N. Y. Tanisa, S. Ahmed, F. Shahriar, and M. M. Haque, "Upcycling prawn shells: Chitosan–carbon nanotube nanocomposites with boosted magnetic and electrical properties," Micro Nano Lett. **19**, e12197 (2024).
[45] S. Mehrin, N. Y. Tanisa, R. Awal, M. K. Alam Khan, A. Shaqur, S. Ahmed, S. Islam, and A. Mia, "Efficient bioelectrochemical cell generation and green synthesis of silver nanoparticles using pomegranate and pineapple peel extracts: A comprehensive characterization study," Adv. Mater. Sci. Eng. **2024**, 6681559.
[46] M. P. Gonzalez-Sandoval, A. M. Beesley, M. Miki-Yoshida, L. Fuentes-Cobas, and J. A. Matutes-Aquino, "Comparative study of the microstructural and magnetic properties of spinel ferrites obtained by co-precipitation," J. Alloys Compd. **369**(1–2), 190–194 (2004).
[47] Y. Kinemuchi, K. Ishizaka, H. Suematsu, W. Jiang, and K. Yatsui, "Magnetic properties of nanosize $NiFe_2O_4$ particles synthesized by pulsed wire discharge," Thin Solid Films **407**(1–2), 109–113 (2002).
[48] R. H. Kodama, A. E. Berkowitz, E. J. McNiff, and S. Foner, "Surface spin disorder in ferrite nanoparticles (invited)," J. Appl. Phys. **81**(8), 5552–5557 (1997).
[49] D. S. Mathew and R. S. Juang, "An overview of the structure and magnetism of spinel ferrite nanoparticles and their synthesis in microemulsions," Chem. Eng. J. **129**(1–3), 51–65 (2007).
[50] Z. L. Wang, Y. Liu, and Z. Zhang, *Handbook of Nanophase and Nanostructured Materials: Materials Systems and Applications I* (Kluwer Academic; Plenum, Boston, MA; New York, 2003), Vol. III.
[51] K. Prasad Malla, S. Regmi, A. Nepal, S. Bhattarai, R. J. Yadav, S. Sakurai, and R. Adhikari, "Extraction and characterization of novel natural hydroxyapatite bioceramic by thermal decomposition of waste ostrich bone," Int. J. Biomater. **2020**, 1690178.
[52] I. Abdulrahman, H. I. Tijani, B. A. Mohammed *et al.*, "From garbage to biomaterials: An overview on egg shell-based hydroxyapatite," J. Mater. Chem. **2014**, 802467.
[53] J. L. Manalu, B. Soegijono, and D. J. Indrani, "Characterization of hydroxyapatite derived from bovine bone," Asian J. Appl. Sci. **3**(04), 758 (2015), https://www.ajouronline.com/index.php/AJAS/article/view/2777.